Respiratory Compensation in Projection Imaging Using a Magnification and Displacement Model

Carl R. Crawford,* *Senior Member, IEEE*, Kevin F. King, Cameron J. Ritchie, and J. David Godwin

Abstract— **Respiratory motion during the collection of computed tomography (CT) projections generates structured artifacts and a loss of resolution that can render the scans unusable. This motion is problematic in scans of those patients who cannot suspend respiration, such as the very young or intubated patients. In this paper, we present an algorithm that can be used to reduce motion artifacts in CT scans caused by respiration. An approximate model for the effect of respiration is that the object cross section under interrogation experiences time-varying magnification and displacement along two axes. Using this model an exact filtered backprojection algorithm is derived for the case of parallel projections. The result is extended to generate an approximate reconstruction formula for fan-beam projections. Computer simulations and scans of phantoms on a commercial CT scanner validate the new reconstruction algorithms for parallel and fan-beam projections. Significant reduction in respiratory artifacts is demonstrated clinically when the motion model is satisfied. The method can be applied to projection data used in CT, single photon emmission computed tomography (SPECT), positron emmission tomography (PET), and magnetic resonance imaging (MRI).**

I. Introduction

RESPIRATORY motion during computed tomography (CT) causes artifacts [1], [2] that can mimic disease and lead to misdiagnosis [3]. Large streaks in the direction of the initial position of the X-ray source are caused by a difference in the data collected at the beginning and ends of data acquisition. Motion artifacts are frequent on scans of unconscious or pediatric patients who are breathing spontaneously; however, they occur even on scans of conscious, cooperative patients [4]. Existing methods for reducing respiratory artifacts either modify the scanning protocols or the reconstruction algorithm.

The magnitude of the motion artifacts is affected by the scan time, the temporal relationship between data acquisition and the respiratory cycle, and by the initial angle of the X-ray source. The artifacts can be eliminated by using a scanner with a very short (less than 94 msec) scan time [5]; however, such short scan times lead to lower signal-to-noise ratios than provided by conventional (1-s) scan times [6], and thus conventional scanners are preferred for CT of the chest. Artifacts can be reduced by aligning the initial position of the X-ray source with the primary direction of motion [7], and by centering data acquisition on the midpoint of the quiescent period of respiration [8], [9].

Motion artifacts can also be reduced by modifying the weights applied to the projections before images are reconstructed with a filtered backprojection algorithm. Streaks in the direction of the initial position of the source can be reduced with the *underscan* algorithm [10]. These streaks and other artifacts can also be reduced by segmenting the data into a set of overlapping *halfscans* [11] and choosing the image with the fewest motion artifacts; however, this method exposes the patient to unnecessary radiation.

Respiratory artifacts have been reduced in magnetic resonance imaging (MRI) by modifying the reconstruction algorithm [12]–[15]. These algorithms are based on a parametric model for the respiratory motion. The basis of the model is the assumption that respiration causes the object cross section under interrogation to experience time-varying magnification and displacement along two axes. The parametric respiration model of the MRI methods can be applied to CT; however, the actual correction technique cannot be used because CT collects data in Fourier-space along spokes, whereas MRI usually uses a rectilinear trajectory.

In this paper, we derive a parallel-beam filtered backprojection algorithm that accounts for respiratory motion using the time-varying magnification model that is used for MRI reconstruction. The parallel-beam result is extended to generate an approximate reconstruction formula for fan-beam projections. Using computer simulations and volunteer scans, we show that the new method eliminates motion artifacts when the parametric model is satisfied.

This paper is organized as follows. First we describe the parametric model and derive the parallel-beam reconstruction formula in Sections II and III. The parallel-beam result is extended to fan-beam projections in Section IV. Computer simulations and volunteer scans are presented in Section V. Finally, we discuss limitations and possible extensions to the new reconstruction method in Section VI.

II. Parametric Motion Model

A simplified cross section of a patient lying supine in a CT scanner is shown in Fig. 1, where the patient's back is resting on the scan table at (x_p, y_p). We assume that respiration causes a time-varying magnification, denoted m_x and m_y, about the x

Manuscript received February 8, 1995; revised February 9, 1996. The Associate Editor responsible for coordinating the review of this paper and recommending its publication was A. Louis. *Asterisk indicates corresponding author.*

*C. R. Crawford was with General Electric Medical Systems, Milwaukee, WI 53203 USA. He is now with Analogic Corporation Peabody, MA 01960 USA (e-mail: ccrawford@analogic.com).

K. F. King is with General Electric Medical Systems, Milwaukee, WI 53203 USA.

C. J. Ritchie was with the Department of Radiology, University of Washington, Seattle, WA 98195 USA. He is now with Imatron, Inc., South San Francisco, CA 94080 USA.

J. D. Godwin is with the Department of Radiology, University of Washington, Seattle, WA 98195 USA.

Publisher Item Identifier S 0278-0062(96)04240-1.

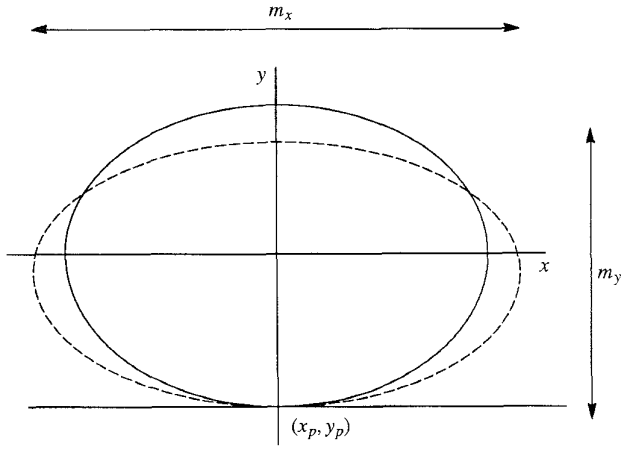

Fig. 1. Outline of cross section of a patient's chest during respiration. The solid and dashed lines represent different samples in the respiratory cycle. Respiration is modeled by time-varying magnification, m_x and m_y, about the x and y axes, respectively, with the fulcrum at (x_p, y_p).

and y axes, respectively, with the fulcrum of the magnification at (x_p, y_p). Let $f(x, y)$ be the cross section to be reconstructed (solid line in Fig. 1). Mathematically, the time varying cross section, $f'(x, y)$, is given by

$$f'(x, y) = f(\alpha_x + \beta_x x, \alpha_y + \beta_y y) \tag{1}$$

where β_x and β_y are related to the magnification factors, m_x and m_y, and α_x and α_y are shift factors. These four parameters are related to the parameters shown in Fig. 1 as follows:

$$\begin{aligned} \beta_x &= m_x^{-1} \\ \beta_y &= m_x^{-1} \\ \alpha_x &= x_p(1 - \beta_x) \\ \alpha_y &= y_p(1 - \beta_y). \end{aligned} \tag{2}$$

The four scaling parameters, $\alpha_x, \beta_x, \alpha_y$, and β_y, are functions of time. We assume that the gantry rotates at constant angular velocity during data acquisition. Therefore, the scaling parameters are also functions of the gantry rotational position. The scaling parameters are not a function of the detector position within a projection because it is assumed that the time required to acquire a projection is short in comparison to the period of motion.

III. Parallel-Beam Reconstruction

We now derive a filtered backprojection reconstruction algorithm for projections acquired during time-varying magnification and displacement. A parallel projection of $f'(x, y), p'(\theta, t)$, at gantry rotational position θ and projection distance t is given by

$$p'(\theta, t) = \int_{-\infty}^{\infty} \int_{-\infty}^{\infty} f'(x, y)\delta(t - x\cos\theta - y\sin\theta)\, dx\, dy \tag{3}$$

where $\delta(t)$ is the Dirac-delta function. Using (1) and (3), the Fourier transform of $p'(\theta, t), S'(\theta, \omega)$ is

$$\begin{aligned} S'(\theta, \omega) = \int_{-\infty}^{\infty} & f(\alpha_x + \beta_x x, \alpha_y + \beta_y y) \\ & \cdot e^{-j2\pi\omega(x\cos\theta + y\sin\theta)}\, dx\, dy. \end{aligned} \tag{4}$$

Using the following change of variables

$$\begin{aligned} x' &= \alpha_x + \beta_x s \\ y' &= \alpha_y + \beta_y y \end{aligned} \tag{5}$$

(4) becomes

$$\begin{aligned} S'(\theta, \omega) = \int_{-\infty}^{\infty} & \frac{f(x, y)}{\beta_x \beta_y} \exp\left[-j2\pi\omega\left(\frac{x}{\beta_x}\cos\theta + \frac{y}{\beta_y}\sin\theta\right)\right] \\ & \cdot \exp\left[j2\pi\omega\left(\frac{\alpha_x}{\beta_x}\cos\theta + \frac{\alpha_y}{\beta_y}\sin\theta\right)\right] dx\, dy. \end{aligned} \tag{6}$$

Let $F(u, v)$ be the two-dimensional (2-D) Fourier transform of $f(x, y)$. Then it follows from (6) that

$$\begin{aligned} S'(\theta, \omega) = & \frac{\exp\left[j2\pi\omega\left(\frac{\alpha_x}{\beta_x}\cos\theta + \frac{\alpha_y}{\beta_y}\sin\theta\right)\right]}{\beta_x \beta_y} \\ & \cdot F\left(\frac{\omega\cos\theta}{\beta_x}, \frac{\omega\sin\theta}{\beta_y}\right). \end{aligned} \tag{7}$$

This equation is a version of the Fourier Slice Theorem in the case of projections acquired from a magnified and shifted object function. It says that the Fourier transform of the projection at gantry position θ is proportional to a spoke of the 2-D Fourier transform of the object function at angle

$$\theta' = \tan^{-1}\left(\frac{\beta_x}{\beta_y}\tan\theta\right). \tag{8}$$

The inverse Fourier transform of $F(u, v)$, is given by

$$f(x, y) = \int_{-\infty}^{\infty} \int_{-\infty}^{\infty} F(u, v) e^{j2\pi(ux + vy)}\, du\, dv. \tag{9}$$

Consider the following change of variables

$$\begin{aligned} u &= \frac{\omega}{\beta_x}\cos\theta \\ v &= \frac{\omega}{\beta_y}\sin\theta. \end{aligned} \tag{10}$$

Using (10), (9) becomes

$$\begin{aligned} f(x, y) = \int_0^{\pi} \int_{-\infty}^{\infty} & F\left(\frac{\omega\cos\theta}{\beta_x}, \frac{\omega\sin\theta}{\beta_y}\right) \frac{|\omega| g(\theta)}{\beta_x \beta_y} \\ & \cdot \exp\left[j2\pi\omega\left(\frac{x}{\beta_x}\cos\theta + \frac{y}{\beta_y}\sin\theta\right)\right] d\omega\, d\theta \end{aligned} \tag{11}$$

where

$$g(\theta) = \left|1 + \frac{\sin 2\theta}{2}\left(\frac{\beta_x'}{\beta_x} - \frac{\beta_x'}{\beta_y}\right)\right| \tag{12}$$

and where β_x' and β_y' are the derivatives of β_x and β_y with respect to θ. When (7) is substituted into (11), (11) reduces to

$$f(x, y) = \int_0^{\pi} q_\theta(t')\, d\theta \tag{13}$$

where

$$q_\theta(t) = g(\theta) \int_{-\infty}^{\infty} S'(\theta, \omega)|\omega| e^{j2\pi\omega t}\, d\omega \tag{14}$$

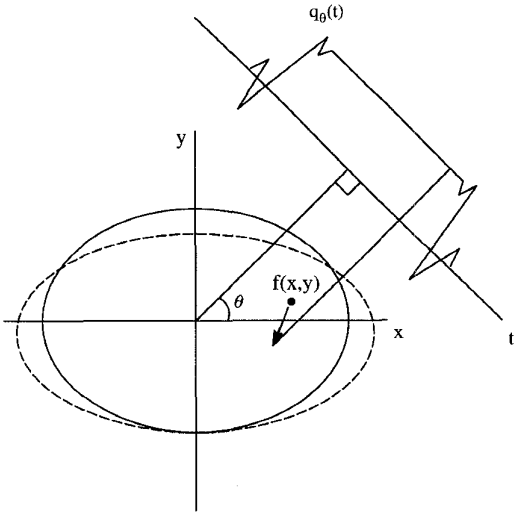

Fig. 2. Contribution of filtered projection, $q_\theta(t)$, to a pixel located at (x, y). The sample in the projection is based on where the pixel was during projection acquisition.

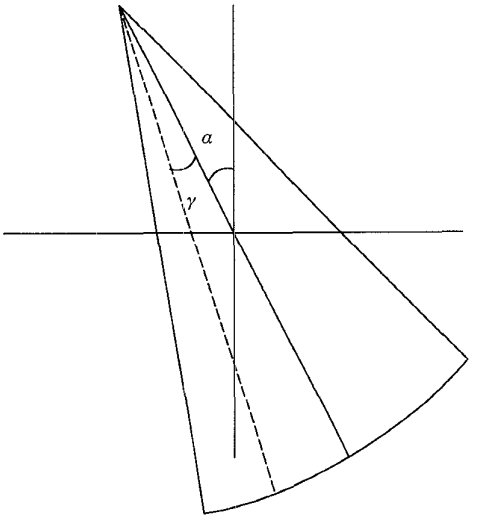

Fig. 3. Geometry of fan-beam projections, where γ is the angle subtended by a detector and α is the projection (gantry) angle.

and where

$$t' = \left(\frac{x-\alpha_x}{\beta_x}\right)\cos\theta + \left(\frac{y-\alpha_y}{\beta_y}\right)\sin\theta. \tag{15}$$

Equation (13) represents a filtered backprojection formula for the reconstruction of parallel-beam projections that are acquired from a magnified and shifted object function. The formula is valid for reconstructing any point in the xy plane. Projections are filtered as they would be with conventional filtered backprojection, but they are then weighted by $g(\theta)$, as given in (12). The value of the weighted, filtered projection at the location given by t', given in (15), is then accumulated for each projection. The new formula is basically the same as conventional reconstruction with the exception that the value of t' is calculated from the location of the pixel (x, y) at the time each projection is acquired as shown in Fig. 2.

IV. Fan-Beam Reconstruction

We now extend the parallel-beam result to fan-beam projections. The fan-beam projections are collected from a curved detector as shown in Fig. 3. Although not shown here, a reconstruction formula for projections collected from a flat detector can be derived using the techniques shown in this Section.

Let $r'(\alpha, \gamma)$ be the fan-beam projection of the magnified and shifted object function $f'(x, y)$. The variable α is the rotational position of the gantry and γ is the detector angle. The parallel-beam and fan-beam projections are related as follows

$$p'(\theta, t) = r'(\alpha, \gamma) \tag{16}$$

for

$$\begin{aligned} t &= D\sin\gamma \\ \theta &= \alpha + \gamma \end{aligned} \tag{17}$$

where D is the the source-to-center distance. In practice, when a third-generation architecture is employed, the four scaling parameters, $\alpha_x, \beta_x, \alpha_y$, and β_y, are functions of α but not γ. We make the assumption that the magnification and shift factors are slowly varying with respect to the gantry's rotational position. Therefore, if the fan-beam projections were rebinned into parallel projections according to (16), the resulting parallel projections have magnification and shift factors that are independent of t, but dependent on θ.

The reconstruction formula for magnified and shifted parallel projections, given in (13), can be written as follows

$$\begin{aligned} f(x,y) = \frac{1}{2}\int_0^{2\pi}\int_{-\infty}^{\infty} & p'(\theta,t)g(\theta) \\ & \cdot h\left(\left[\frac{x-\alpha_x}{\beta_x}\right]\cos\theta + \left[\frac{y-\alpha_y}{\beta_y}\right]\sin\theta - t\right) dt\, d\theta \end{aligned} \tag{18}$$

where $h(t)$ is the the inverse Fourier transform of $|\omega|$. Now consider the reconstruction formula (18) after the change of variables given in (17). The reconstruction formula in the $\alpha\gamma$ space is given by

$$\begin{aligned} f(x,y) = \frac{1}{2}\int_0^{2\pi}\int_{-\infty}^{\infty} & r'(\alpha,\gamma)g(\alpha+\gamma)D\cos\gamma \\ & \cdot h\left(\left[\frac{x-\alpha_x}{\beta_x}\right]\cos(\alpha+\gamma) + \left[\frac{y-\alpha_y}{\beta_y}\right]\right. \\ & \left. \cdot\ \sin(\alpha+\gamma) - D\sin\gamma\right) d\gamma\, d\alpha. \end{aligned} \tag{19}$$

The argument of filter h in (19) can be simplified to

$$L\sin(\gamma' - \gamma) \tag{20}$$

where

$$\begin{aligned} \gamma' &= \tan^{-1}\left(\frac{E_1}{E_2}\right) \\ L^2 &= E_1^2 + E_2^2 \end{aligned} \tag{21}$$

and where

$$\begin{aligned} E_1 &= X\cos\alpha + Y\sin\alpha \\ E_2 &= X\sin\alpha - Y\cos\alpha + D \end{aligned} \tag{22}$$

and finally, where

$$X = \frac{x - \alpha_x}{\beta_x}$$
$$Y = \frac{y - \alpha_y}{\beta_y}. \tag{23}$$

The reconstruction kernel, $h(t)$, satisfies [16]

$$h(at) = \frac{1}{a^2} h(t). \tag{24}$$

Therefore

$$h(L\sin(\gamma' - \gamma)) = \left(\frac{\gamma}{L\sin\gamma}\right)^2 h(\gamma' - \gamma). \tag{25}$$

Now we substitute (25) into (19) which yields

$$f(x,y) = \int_0^{2\pi} \frac{1}{L^2} q_c(\alpha, \gamma')\, d\alpha \tag{26}$$

where

$$q_c(\alpha,\gamma) = \int_{-\infty}^{\infty} G(\lambda,\alpha) r'(\alpha,\lambda) H(\gamma - \lambda)\, d\lambda \tag{27}$$

and where

$$G(\gamma,\alpha) = \tfrac{1}{2} g(\alpha + \gamma) D\cos\gamma \tag{28}$$

and also where

$$H(\gamma) = \left(\frac{\gamma}{L\sin\gamma}\right)^2 h(\gamma). \tag{29}$$

Equation (26) represents a filtered backprojection formula for the reconstruction of fan-beam projections collected from a magnified and shifted object. The formula is basically the same as conventional reconstruction from fan-beam projections. The major difference is the location of the filtered projection, γ', is calculated using the location of a pixel at the time the projection is acquired.

V. Results

Computer simulations were run to study the performance of the new reconstruction algorithms. A set of circles was simulated as shown in Figs. 4(a) and 5(a). The pivot point (x_p, y_p) is the posterior edge of the largest circle. The specifics of the magnification model are

$$m_x = 1 - \sin(\zeta/2)/20$$
$$m_y = 1 + \sin(\zeta/2)/5$$
$$x_p = 0 \text{ mm}$$
$$y_p = -20 \text{ mm} \tag{30}$$

where ζ is the gantry's rotational position, which corresponds to θ for parallel-beam projections and α for fan-beam projections. The model is based on the assumption that respiration causes a relatively large magnification in the anterior–posterior (AP) direction. A smaller amount of lateral motion is incorporated into the model. Two hundred and fifty-six projections were generated assuming a point source and a point detector. Two hundred and fifty-six samples per projection were generated. A 50-mm field-of-view was used. Images were reconstructed using a 256^2 matrix.

Figs. 4 and 5 show the reconstructions obtained with parallel-beam and fan-beam projections, respectively. Results

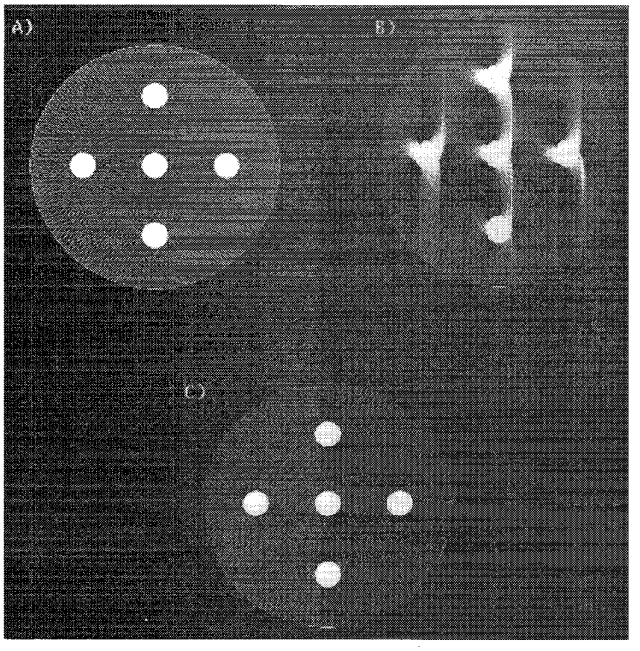

Fig. 4. Reconstructions with parallel-beam projections: a) no motion, b) with simulated motion but without correction, and c) with motion correction.

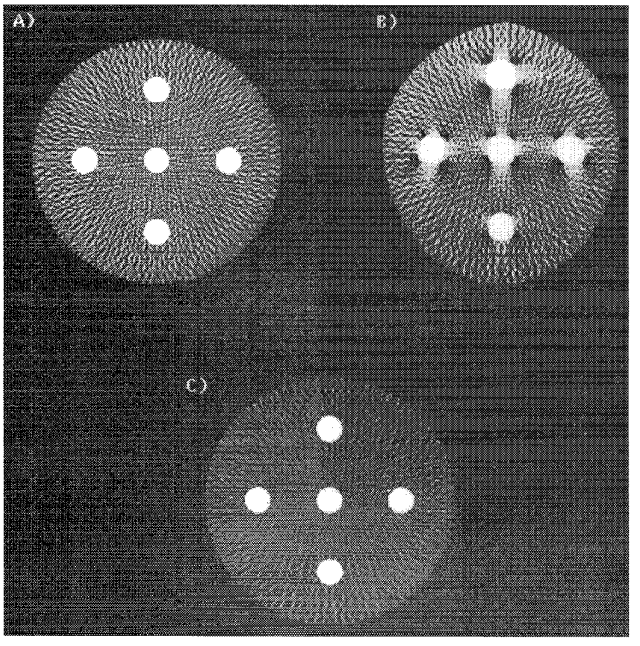

Fig. 5. Reconstructions with fan-beam projections: (a) no motion, (b) with simulated motion but without correction, and (c) with motion correction.

are shown with and without correction, and for projections obtained without magnification. From Figs. 4(b) and 5(b), it is seen that the top (anterior) circle is degraded the most. The circle at the bottom (posterior) is only slightly distorted because it is only affected by the β_x term which is relatively small. Figs. 4(c) and 5(c) show that the modified reconstruction algorithms remove the majority of the artifacts caused by the magnification model. Close inspection of the images on a workstation shows that the fan-beam

reconstructions suffer from some low-frequency shading artifacts. We attribute this shading to the assumption that the magnification is independent of the detector position in a parallel-beam projection that would result from rebinning the fan-beam projections.

We also scanned two plexiglass, cone-shaped phantoms on a 9800 Hilight Scanner (GE Medical Systems, Milwaukee, Wisconsin). The motion of the cones through the imaging plane was synchronized to data collection using computer control [17]. One cone was solid and the other had a cylindrical portion removed from the cone's axis of symmetry. The resulting images (not shown) demonstrate that the the solid cone could be reconstructed without motion artifacts. However, the other cone generated artifacts, as expected, from the cylindrical cutout because it did not satisfy the motion model.

A healthy male volunteer was scanned on the 9800 Hilight Scanner. Scans were obtained at one level in the chest and one level in the liver. At each level, a stationary scan was obtained by suspending respiration during data acquisition. A number of scans were acquired while the volunteer was breathing during the scan. The scan times were relatively long (up to 8 s) in order to emphasize the artifacts caused by respiration. Respiration was monitored with a measuring device placed above the volunteer. The device recorded the AP motion on one point on the volunteer's chest near the location of the scan. The motion model was that the volunteer's back was the pivot point, no lateral magnification occurred and the AP magnification was derived from the output of the measuring device.

Fig. 6 shows the stationary, uncorrected, and corrected results of scans through the lungs. These images show excellent correction of portions of the anterior chest wall. Little correction in the heart was seen, although vessels close to the heart were improved (some superposition was still apparent). The heart wall showed correction on the volunteer's left side but not on the right. Vessels in the volunteer's right chest that showed doubling were almost superimposed. However, in the left chest, some vessels appeared to be farther apart after correction, suggesting that too much correction was applied. This overcorrection can be seen in the right-side posterior chest wall. In the lung we suspect that superior–inferior (SI) motion was minimal, and that the majority of the problems in correction was caused by inaccurate in-plane motion modeling.

The images in the liver (not shown) demonstrate that artifacts along the anterior chest wall were reduced. However, the artifacts in the liver and around the ribs were not eliminated. Respiration causes significant SI displacement of the liver [18]. The ribs do not satisfy the model because they pivot about the spine. Therefore, it is not too surprising that the method did not hold for the liver because our simple in-plane expansion model does not address SI motion. It might be possible to remove the rib artifacts by applying a metal-artifact-removal algorithm [19] to the ribs.

VI. Conclusions

The computer simulations and the phantom scans demonstrate the validity of our new reconstruction method. Motion

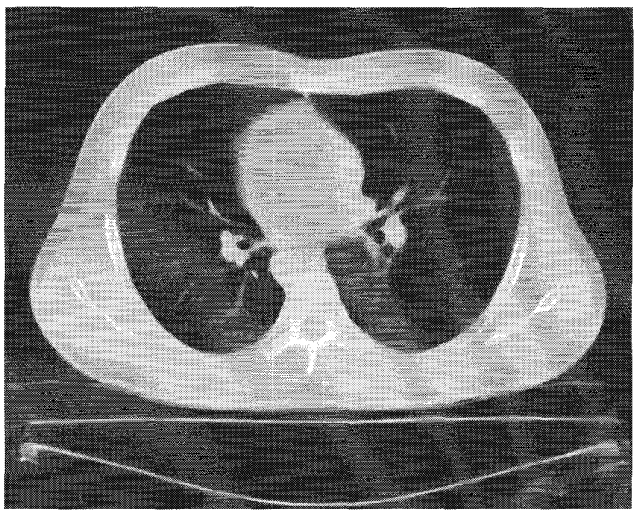

(a)

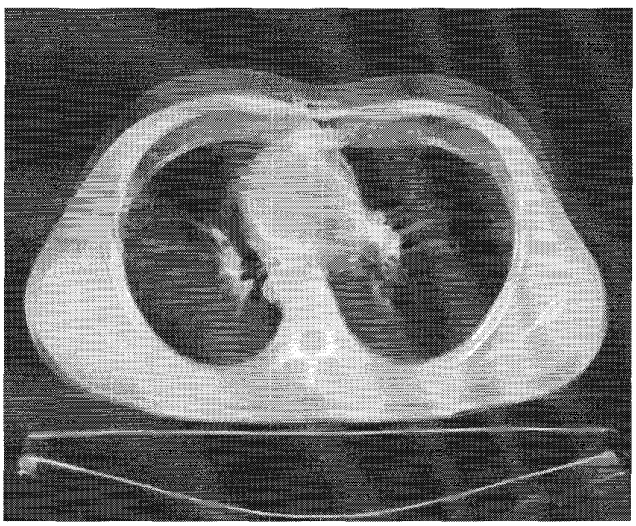

(b)

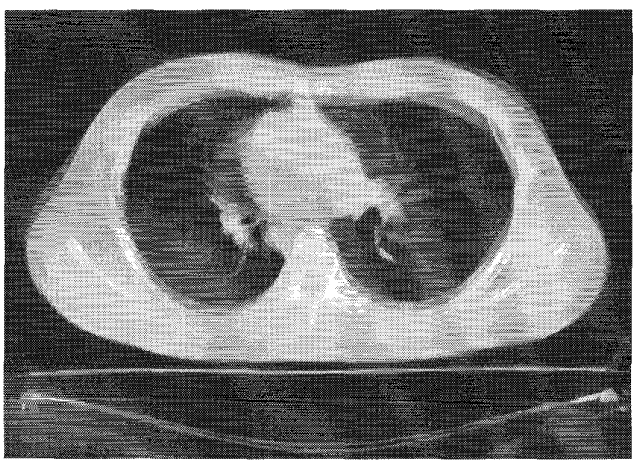

(c)

Fig. 6. Reconstructions of volunteer: (a) with suspended respiration, (b) with respiration but without correction, and (c) with motion correction.

artifacts were reduced more in the chest scans than in the liver scans because motion in the chest better satisfies our model. Additional artifact reduction was obtained in the lung scans when we applied the model to small regions and adjusted the model parameters locally. This adjustment was done because the present, time-varying magnification model is not accurate enough for the complete chest cavity. Preliminary results have shown that additional artifact reduction is obtained when this model is applied on a pixel-by-pixel basis [20], [21].

The model given in (1) predicts that the object will lose mass when magnification occurs. The model, therefore, correctly describes the computer simulations and the scanning of the cone. However, it is not clear if the model is adequate for the effects of respiration. One could argue that mass is preserved and density changes. If this were the case, the acquired projections would have to be scaled by $\beta_x\beta_y$ to keep the mass constant. Computer simulations showed that the majority of the artifact reduction from the new method occurs because the contribution of the filtered projection is calculated from where a pixel was at the time a projection was acquired. Therefore, the question of whether to preserve mass or density is not that significant. We assumed constant density for the volunteer scans.

The new reconstruction method can be combined with halfscan [10] and underscan [11] to obtain additional artifact reduction. Exact halfscan and underscan reconstruction formulas cannot be derived in the case of projections acquired with magnification because halfscan and underscan rely on a set of fan-beam projections containing values for duplicate integration paths. Because the object is changing during the collection of projections, the projection set will not necessarily contain the duplicate information. Even though the halfscan and underscan algorithms could not be derived, computer simulations showed that respiratory artifacts are reduced; however, some low-frequency shading artifacts are introduced. Additional clinical tests are required to determine if the reduction of respiratory artifacts is more important than the low-frequency shading.

In normal filtered backprojection for parallel projections, the Fourier Slice Theorem says that projections acquired over a span of π will fill the 2-D Fourier transform of the object. A consequence of (8) is that θ' is only guaranteed to be equal to θ for θ equal to zero and $\pi/2$. Therefore, we are assured that the Fourier space of the object will be sampled exactly one time only if projections are acquired with the source initially parallel to the x or y axes. Otherwise, part of Fourier space will be missing or duplicated. This result is consistent with existing motion reduction methods in which the initial position of the X-ray is aligned with the dominant motion in a subject under examination [7]. The commercial scanner that we used for our testing starts the source on the AP axis because respiratory motion is more pronounced along the vertical axis.

In conclusion, we have derived a filtered backprojection algorithm that corrects for artifacts generated by objects experiencing time-varying magnification. When the in-plane effects of respiration approximate the magnification model, we demonstrated with clinical scans that motion artifacts caused by respiration can be reduced. Finally, the method can be applied to other modalities that acquire projections such as SPECT and PET.

ACKNOWLEDGMENT

The authors thank G. Glover, S. Flax, J. Hsieh, H. Hu, R. Kinsinger, H. Levy, and A. Lonn for feedback.

REFERENCES

[1] L. A. Shepp, S. K. Hillal, and R. A. Schulz, "The tuning fork artifact in computerized tomography," *Comput. Graph. Imag. Processing*, vol. 10, pp. 246–255, 1979.
[2] J. R. Mayo, N. L. Müller, and R. M. Henkelman, "The double-fissure sign: A motion artifact on thin-section CT scans," *Radiol.*, vol. 165, pp. 580–581, 1987.
[3] R. D. Tarver, D. J. Conces, Jr., and J. D. Godwin, "Motion artifacts on CT simulate bronchiectasis," *Amer. J. Radiol.*, vol. 151, pp. 1117–1119, 1988.
[4] D. E. Dupuy, P. Costello, and C. P. Ecker, "Spiral CT of the pancreas," *Radiol.*, vol. 183, pp. 815–818, 1992.
[5] C. J. Ritchie, J. D. Godwin, C. R. Crawford, W. Stanford, H. Anno, and Y. Kim, "Minimum scan speeds for suppression of motion artifacts in computed tomography," *Radiol.*, vol. 185, pp. 37–42, 1992.
[6] R. G. Gould, "Principles of ultrafast computed tomography: Historical aspects, mechanisms of action, and scanner characteristics," in *Ultrafast Computed Tomography in Cardiac Imaging: Principles and Practice*, W. Stanford and J. A. Rumberger, Eds. Mount Krisco, NY: Futura, 1992, pp. 1–15.
[7] C. R. Crawford and N. J. Pelc, "Method for reducing motion induced artifacts in projection imaging," U. S. Patent 4 994 965, 1991.
[8] C. R. Crawford, J. D. Godwin, and N. J. Pelc, "Reduction of motion artifacts in computed tomography," in *Proc. IEEE Eng. Med. Biol. Soc.*, vol. 11, pp. 485–486, 1989.
[9] C. J. Ritchie, J. Hsieh, M. F. Gard, J. D. Godwin, Y. Kim, and C. R. Crawford, "Predictive respiratory gating: A new method to reduce motion artifacts in CT," *Radiol.*, vol. 190, pp. 847–852, 1994.
[10] N. J. Pelc and G. H. Glover, "Method for reducing image artifacts due to projection measurement inconsistencies," U.S. Patent 4 580 219, 1986.
[11] D. L. Parker, "Optimal short scan convolution reconstruction for fan-beam CT," *Med. Phys.*, vol. 9, pp. 254–257, 1982.
[12] J. J. M. Cuppen, J. P. Groen, J. J. E. In den Kleef, and H. A. Tuithof, "Reduction of motion artifacts by data processing," in *Proc. Soc. Magn. Reson. Med.*, 1985, vol. 4, pp. 962–963.
[13] E. M. Haacke and J. L. Patrick, "Reducing motion artifacts in two-dimensional Fourier transform imaging," *Magn. Reson. Imag.*, vol. 4, pp. 359–376, 1986.
[14] R. L. Ehman and J. P. Felmlee, "Adaptive technique for high-definition MR imaging of moving structures," *Radiol.*, vol. 173, pp. 255–263, 1989.
[15] E. Atalar and L. Onural, "A respiratory motion artifact reduction method in magnetic resonance imaging of the chest," *IEEE Trans. Med. Imag.*, vol. 10, no. 1, pp. 11–24, 1991.
[16] A. C. Kak and M. Slaney, *Principles of computerized tomographic imaging*. New York: IEEE Press, 1987, p. 82.
[17] C. J. Ritchie, E. Peterson, D. Yee, Y. Kim, J. D. Godwin, and C. R. Crawford, "A 3-D motion control system for simulation of CT motion artifacts," in *Proc. IEEE Eng. Med. Biol. Soc.*, 1989, vol. 11, pp. 487–488.
[18] O. L. Wade, "Movements of the thoracic cage and diaphragm in respiration," *J. Physiol.*, vol. 124, pp. 193–212, 1954.
[19] G. H. Glover and N. J. Pelc, "An algorithm for the reduction of metal clip artifacts in CT reconstructions," *Med. Phys.*, vol. 8, no. 6, pp. 799–807, 1981.
[20] C. J. Ritchie, Y. Kim, C. R. Crawford, and J. D. Godwin, "CT motion artifact correction using pixel-specific backprojection," in *Proc. IEEE Eng. Med. Biol. Soc.*, 1992, vol. 14, pp. 1782–1783.
[21] C. J. Ritchie, C. R. Crawford, J. D. Godwin, K. F. King, and Y. Kim, "Correction of computed tomography motion artifacts using pixel-specific backprojection," this issue, pp. 333–342.